Investigating the Influence of Pore Wall – Water Interactions on Proton Conductivity within Metal-Organic Nanotubes Using Electrochemical Impedance Spectroscopy

*Tiron H.L. Jahinge and Tori Z. Forbes**

Department of Chemistry, University of Iowa, Iowa City, IA 52242

*Corresponding Author; tori-forbes@uiowa.edu

KEYWORDS

Metal organic nanotubes, Surface polarity, Proton conductivity, Nanoconfinement, Electrochemical impedance spectroscopy

ABSTRACT

Water-mediated proton conductivity in nanoporous materials is influenced by channel water ordering and the hydrophobicity/hydrophilicity of interior walls, making metal-organic nanotubes (MONTs) useful systems for exploring these relationships due to their high crystallinity and tunable hydrophobicity. In the current study, we utilize electrochemical impedance spectroscopy to explore the proton conductivity on two metal organic nanotubes (UMONT and Cu-LaMONT) with weak hydrophobic behavior that possess extended water networks within the 1-D channels. Measurements performed at 95% RH and 20 °C indicated values of 1.63×10^{-4} Scm^{-1} for UMONT and 3.80×10^{-4} Scm^{-1} for Cu-LaMONT, which is lower than values for walls with acidic, hydrophilic functional groups or nanotubular materials with strictly hydrophobic behavior. Proton conductivity decreased sharply with lower humidity, with Cu-LaMONT being more sensitive to humidity changes. At low temperatures, UMONT outperformed Cu-LaMONT due to its well-established hydrogen bonding network and hydrophobic interior. The anisotropic nature of proton conduction was also confirmed through pelletized powder sample analysis, emphasizing that the conductivity occurs through the water networks located within the 1-D MONT channels. Our findings emphasize the importance of understanding water-pore interactions and the resulting proton conductivity mechanisms to understand complex systems and design advanced materials.

INTRODUCTION

Water conductivity is of particular interest within nanoporous biological and engineered systems where water molecules allow protons to move swiftly from one water molecule to another.[1] Generally, two types of proton conduction mechanisms, Grotthuss and vehicle, are utilized to explain this process. In the Grotthuss mechanism, formation or cleavage of H-bonds between a hydronium ion and water molecules or other H-bonded liquids occurs,[2] with protons hopping from one site to another site along the local arrangements. With the vehicle mechanism, protons combine with carrier molecules (i.e. H_2O or NH_3) to assist in diffusion through the solvent,[3] and the proton transfer occurs via the sequential breaking and formation of hydrogen bonds. In either mechanism, the presence of water-filled pores creates an environment where protons can travel efficiently, exploiting the collective behavior of confined molecules.[4] This process is important in biological processes, such as proton pumping in cellular respiration,[4a] as well as in emerging technologies like proton exchange membrane fuel cells,[5] where it plays a pivotal role in facilitating the conversion of chemical energy into electrical energy.

Within 1-D nanoporous materials, the water networks are confined and can interact with the channel walls, resulting in diverse structural arrangements that can impact the hydrogen bonding and proton conductivity along the pore. Water within these pore spaces can possess highly ordered configurations with similarities to ice-like topologies or more disordered, amorphous states.[6] The level of water ordering critically impacts conductivity because well-ordered structures with defined hydrogen-bonded pathways tend to facilitate rapid proton transport[6d, 7] and disordered arrangements impede conductivity[8] due to irregular pathways and weaker hydrogen bonding networks. The level and type of water ordering can be linked to the overall diameter of the channel and the levels of hydrophobicity of the interior channel wall.[6d, 9] Typically water ordering within

materials occurs most readily when the pore diameters range between 0.8-2 nm but the structural details are determined by the interactions between the confined water molecules and the inner channel walls.[6d, 10] Within hydrophilic systems, the nanoconfined water molecules can form hydrogen bonds with functional groups on pore wall and create anchor points that cause lateral movement of protons on the surface of a membrane.[11] This enhanced polarity-driven interaction between water and the channel may promote efficient proton transport through the porous network.[12] Hydrophobic surfaces tend to repel water molecules so that the water molecules within the confined space will form extensive water networks among themselves.[6d] This leads to ice-like structures within the channel walls that are well-ordered but may not have much mobility for the protons to move through the channel. However, Freier *et al.* observed that ordered water chains within hydrophobic regions of proteins still promoted proton conductivity[13] and additional studies found that Grotthuss-type transfer occurred as long as there was strong hydrogen bonding between water molecules at the uptake site.[2, 14] This intricate relationship underscores the importance of both water ordering and surface characteristics in shaping proton conductivity within nanochannels, but exact details for complex materials with variable hydrophobicity is lacking.

Metal-organic nanotubes (MONTs) represent a promising class of materials for probing the interplay between water ordering, hydrophobicity/hydrophilicity, and proton conductivity in complex nanoconfined spaces that could enhance the design of advanced materials. MONTs are nanotubular structures built on metal nodes connected through organic linkers to create three-dimensional crystalline solids.[15] These materials can be characterized by single-crystal diffraction to obtain, and atomistic understanding of the water ordering and their porosity is suitable for hosting guest molecules, including water. [9c-e, 16] By carefully tuning the structural components of

MONTs, the hydrophobic or hydrophilic properties of the material can be varied, which in turn can influence the interactions of the confined water molecules and diffusion through the system.[16] Previous work on proton conductivity within MONT and related hybrid materials have focused mainly on adding acidic functional groups. However, Otake *et al*. discovered that hydrophobic MONT materials can exhibit high proton conductivity as well, which also aligns with the previous work by Freier *et al*.[6d, 13]

The current study investigated water mediated proton conductivity using two MONT materials (UMONT and Cu-LaMONT) that contain more hydrophobic pore walls and ordered water networks.[9c, 9d] These materials have similar water channels to that reported by Otake *et al*., but more interactions between the confined water molecules and the inner pore wall.[6d] Single-crystal X-ray diffraction was employed to identify the orientation of the one-dimensional nanopores and the nature of the water network, which is pivotal for accurately evaluating the conductivity in these systems.[8, 17] Electrochemical impedance spectroscopy (EIS) was then utilized at different temperatures and relative humidities to determine the conductivity at different conditions. Finally, the activation energy was calculated using the Arrhenius plot derived from temperature study.

RESULTS

MONT materials were synthesized, and crystals were isolated for further crystallographic analysis. Unit cell dimensions matched previously reported values in the literature and the crystal dimensions were measure as 0.194 mm × 0.252 mm × 0.606 mm and 0.362 mm × 0.488 mm × 0.644 mm for UMONT and Cu-LaMONT, respectively. Based upon the analysis performed in the APEX4 software, the crystal morphology was modeled and indexed to determine the orientation of the (001) face (Fig. 1a and 1b).[18] Identifying the orientation of the [001] direction was

important as it represents the channels of the MONT material that contains the nanoconfined water channels. The molecular arrangement of water within metal organic nanotubes plays a vital role in demonstrating the potential for proton conductivity and the structural topologies of the material have been described in previous work.[9c, 9d] Both UMONT and Cu-LaMONT are built from U(VI) or Cu(II)/La(III) metal nodes coordinated by iminodiacetate (IDA) ligands to create the nanotubular structure and well-organized water networks are located within the MONT materials (**Fig**. 1c and 1d). In the case of UMONT, there are two crystallographically distinct water positions (**Fig**. 1e), resulting in the formation of two different hexameric rings that then link into an infinite 1-D array through hydrogen bonding. The water molecules within these structures do not form strong interactions with the pore walls, which enables them to have strong water-water interactions that lead to an Ih ice-like lattice.[9c] Conversely, the water structure in Cu-LaMONT contains a cage-like topology with significant similarities to a network of bicylco-octamers (**Fig**. 1f) that are built from the O3W in the apex positions, with O2WA and O2WB creating the sides of the cage.[9d] This motif is observed within water clusters in the liquid phase, as well as the Ih-Ice structure. A fourth water molecule (O1W) is observed as a pendant to the bicylco-octamer and further bonds to the interior wall of the Cu-LaMONT nanotube through interactions with a hydrophilic amine group.

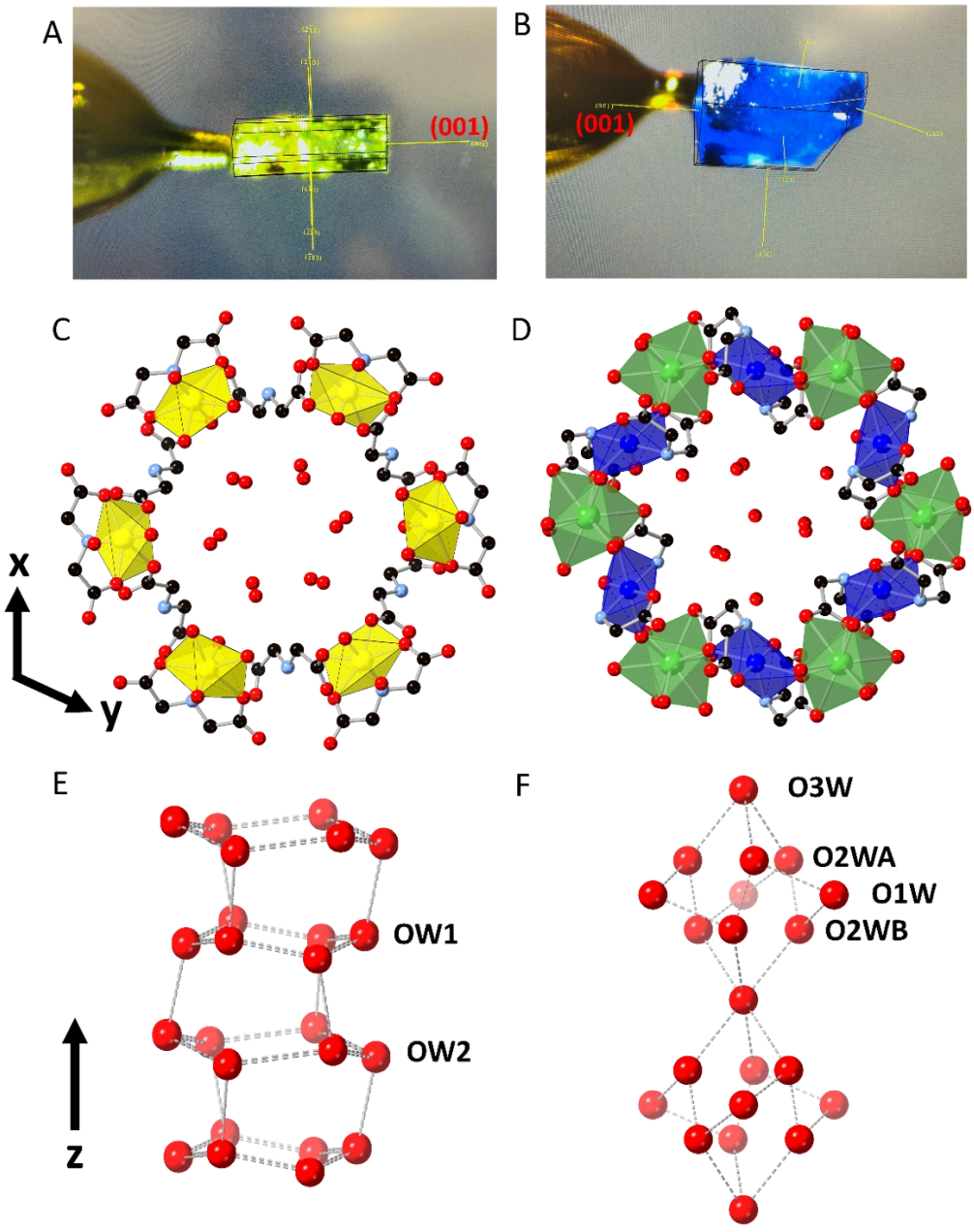

Figure 1. UMONT (a) and Cu-LaMONT (b) single crystals utilized in this study were indexed using the X-ray diffractometer with the [001] direction labeled in red. Ordered nanotubular channels are observed within the UMONT (c) and Cu-LaMONT (d) material and contain

nanoconfined water molecules.[9c, 9d] U, Cu, La, C, N, and O atoms associated with the nanotubular arrays are depicted as yellow, deep blue, green, black, light blue, and red, respectively. H atoms have been removed from the crystal structure for the clarity. Structural topologies for the confined water molecules within UMONT (e) and Cu-LaMONT (f) are depicted using red-spheres with hydrogen bonding networks denoted by dashed lines. Crystallographically unique O atoms are labeled and unlabeled atoms are the symmetry equivalent sites.

AC impedance analysis was performed on large single crystals of the MONT materials along the [001] direction. Proton conductivity values were measured at ambient temperature (25 °C) with 95% RH for UMONT and Cu-LaMONT as 1.27×10^{-4} and 2.89×10^{-4} S cm^{-1}, respectively (**Fig**. 2). We confirmed that the *dc* conductivity is less than the lower limit of measurement, ruling out significant electrical conductivity in the tube. Next, the *ac* impedance spectroscopy was employed and the initial response at low MΩ for both UMONT and Cu-LaMONT within the Nyquist plot suggested the conductivity is protonic in nature.[6d] The obtained experimental impedance spectral data were fitted with the most relevant circuit (SI, Fig. S7) using the AfterMath software (Pine Research) and all impedance data fit well with the same circuit. Proton conductivity values were determined from the low MΩ data (SI, Fig. S8) in the Nyquist plots, and we determined that UMONT and Cu-LaMONT have similar values (1.63×10^{-4} Scm^{-1} for UMONT and 3.80×10^{-4} Scm^{-1} for Cu-LaMONT at 20°C and 95% RH).

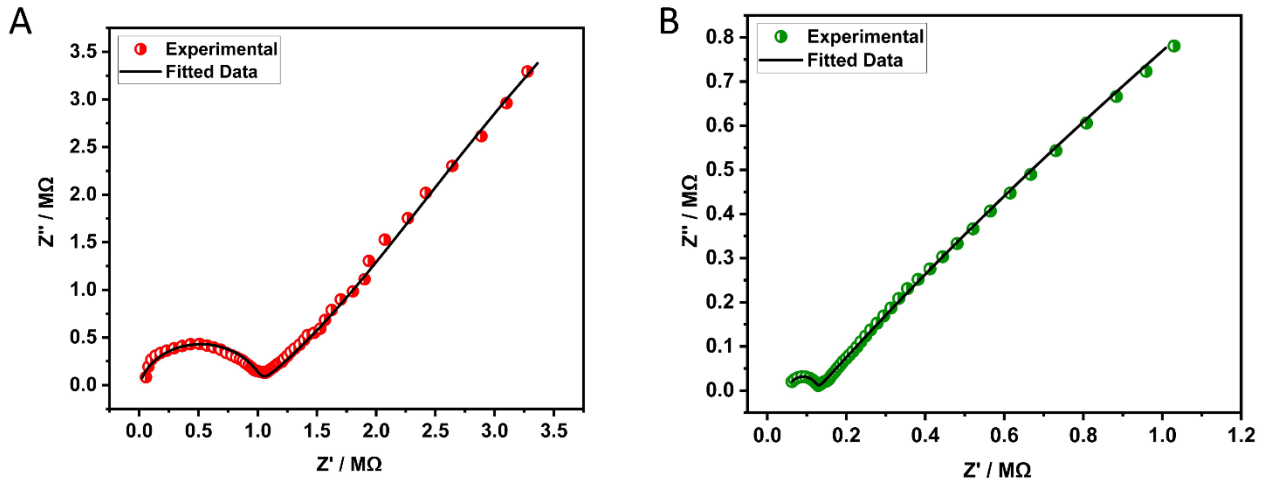

Figure 2. Nyquist plots were generated from AC impedance data of UMONT (a) and Cu-LaMONT (b) at 25 °C and 95% relative humidity.

Previous work also demonstrated that these MONT materials are sensitive to relative humidity so the impacts of this variable on proton conductivity was further explored for this system. [19] Initial experiments were conducted at 95% RH and an equilibrium time of at least 45 minutes because previous work demonstrated that these conditions led to complete filling of the MONT materials.[19-20] Additional ac impedance spectra were obtained at 55, 65, 75, 85% RH values and ambient temperature (25 °C) (**Fig**. 3). These spectra exhibited a notable increase in resistivity within the system, resulting in a concomitant decrease in conductivity at lower RH conditions. When RH was lowered from 95 to 55%, the conductivity in UMONT and Cu-LaMONT decreased from 1.27×10^{-4} and 2.89×10^{-4} Scm^{-1} to 9.72×10^{-7} and 3.53×10^{-7} Scm^{-1}, respectively (SI, Table S2). This reduction in the conductivity highlights the pivotal role played by the water network in facilitating the conduction of protons. Proton conductivity of Cu-LaMONT is more sensitive to the RH value than that of UMONT, evident from a sharp drop in proton conductivity with decreasing humidity (Fig. S9).

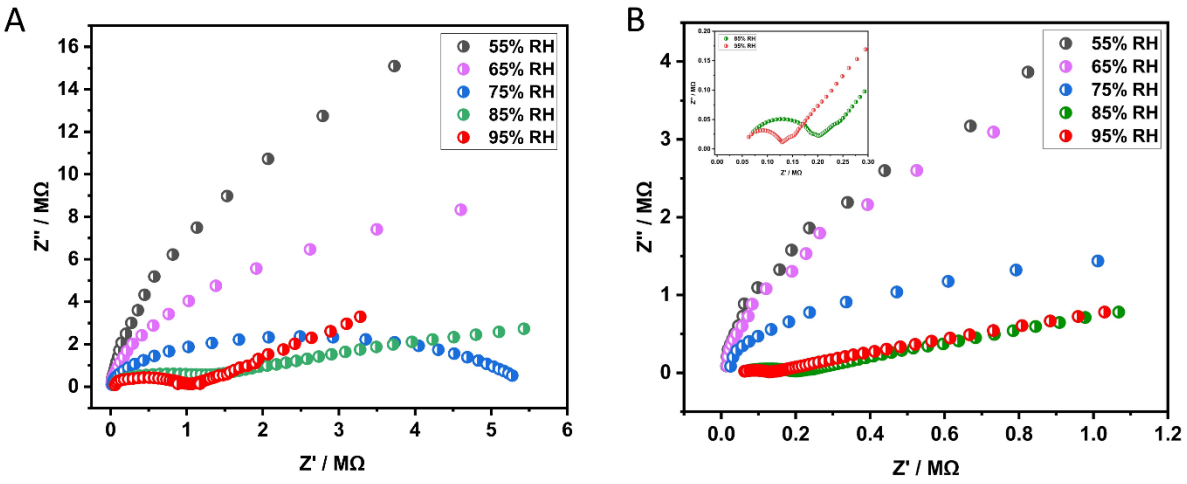

Figure 3. Impedance was plotted for UMONT (a) and Cu-LaMONT (b) under different relative humidity condition. The inset for the Cu-LaMONT highlights the features in the low Z' data for 85 and 95% RH values.

Impact of temperature was also considered by also collecting conductivity measurements between 5 to 45 °C at a constant 95% RH and 45 min equilibrium time (**Fig**. 4). In both UMONT and Cu-LaMONT systems, the proton conductivity values increased from 5 to 20 °C, then decreased when the temperatures reached 40 and 45°C (**Fig**. 4; SI Fig. S10 and 11). Previous work indicated that dehydration of the pore space for both MONT systems occurs when temperatures reach 40-45°C, which explains the sudden change in the impedance at that point.[9c, 9d] The measured conductivity decreased from 1.63×10^{-4} to 3.45×10^{-7} Scm^{-1} for the UMONT system and the value was lowered from 3.80×10^{-4} to 7.14×10^{-7} Scm^{-1} for Cu-LaMONT when the temperature changed from 20 °C to 45 °C (SI, Table S3). Comparing the conductivity values at lower temperature (5°C) for both systems indicates that UMONT has a high value (1.38×10^{-4} Scm^{-1}) than observed in Cu-La MONT (5.72×10^{-6} Scm^{-1}).

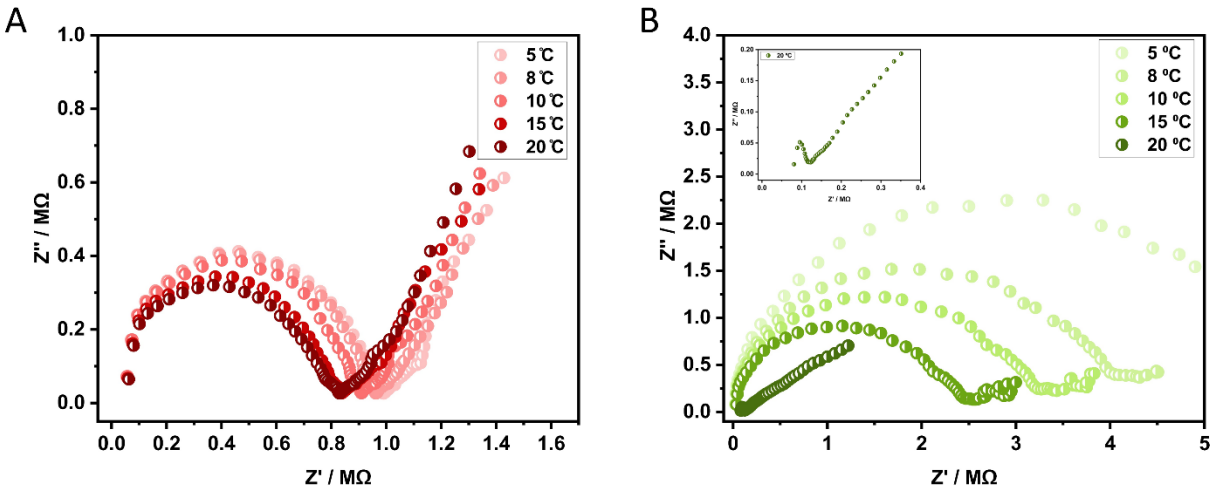

Figure 4. Impedance was plotted for UMONT (a) and Cu-LaMONT (b) at different temperatures. The inset for the Cu-LaMONT highlights the features in the low Z' data for the data collected at 20 °C.

Proton conductivity was also measured on a pelletized powder sample to evaluate the importance of directionality in the system. The powdered samples (SI, Fig S12-13) displayed conductivity values that were significantly lower than the single crystal forms (2.03×10^{-12} Scm^{-1} for UMONT and 1.00×10^{-12} Scm^{-1} for Cu-LaMONT) at 95 % RH and 25 °C. This result indicates that the proton conduction is highly anisotropic, and that the conducting pathway is in the [001] direction. Decreasing the relative humidity for the pelletized powder samples (Fig. S14 and S15) also resulted in a decrease in the conductivity values, which is similar to the trend observed for the single-crystal materials.

To elucidate the proton conduction mechanism, we must ascertain the activation energy (E_a) associated with this process and this value was calculated for UMONT and Cu-LaMONT based on their conductivity measurements at different temperatures. A graphical representation was constructed by plotting the natural logarithm of the product of proton conductivity (σ) and

temperature (T) against the reciprocal of temperature (1000/T) for UMONT and Cu-LaMONT samples. The slope of this plot, as determined by the Arrhenius equation, enables the calculation of the activation energy of proton conductivity. From the Arrhenius equation,

$$\sigma T = \sigma_0 \exp(-E_a / K_b T)$$

Where σ = proton conductivity of the sample; K_b = Boltzmann constant; R = ideal gas constant; T = temperature (K). From this equation, the activation energy for proton conduction for UMONT and Cu-LaMONT was determined as 0.15 and 0.65 eV, respectively (**Fig. 5**).

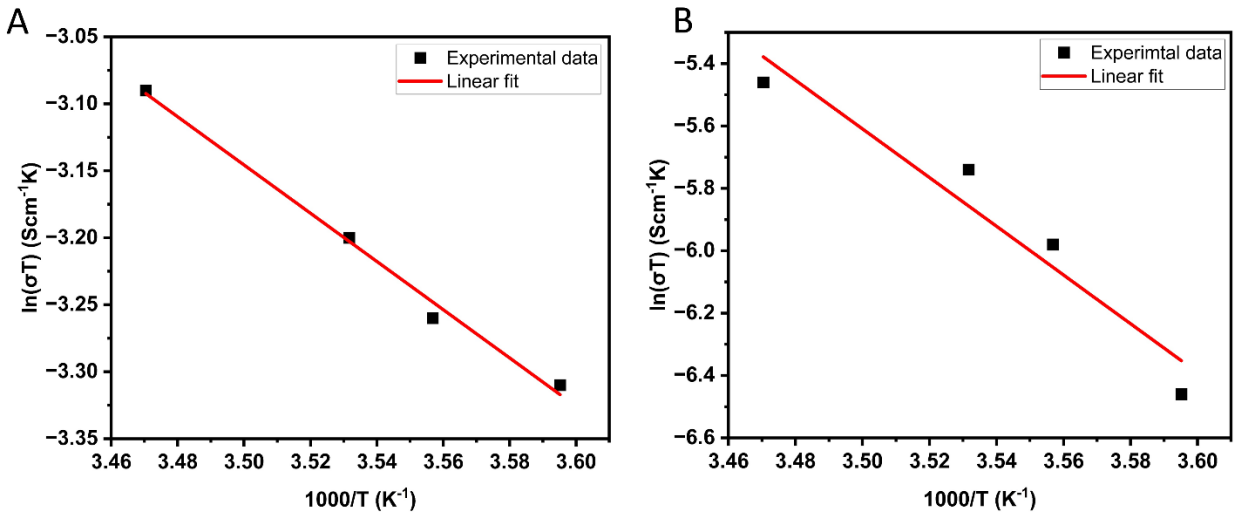

Figure 5. Arrhenius plots for UMONT (a) and Cu-LaMONT (b) were used to determine the activation energy for proton conductivity.

DISCUSSION

To compare the proton conducting efficiency of UMONT and Cu-LaMONT to other materials, we have summarized previously reported data for Nafion, MONTs, and related hybrid material (**Table** 1). In addition, we have catalogued the hydrophobic/hydrophilic functional groups that

are located on the surface of the interior channel walls for each compound to provide additional insights into relationships between the chemistry of the pore and the measured proton conductivity. Conductivity within most of these systems range from 2.3 x 10^{-9} to 1.8 x 10^{-2} S cm^{-1}, with the values we obtained from UMONT and Cu-LaMONT falling in the middle of this range. In general, higher proton conductivity values in hybrid materials can be linked to the presence of hydrophilic acidic groups on the interior of the channel wall, possessing a proton-rich counter ion, and accommodating more water molecules into the nanoporous space. As the inner wall becomes less hydrophilic, the conductivity values decrease although the exception to that rule is the MIL-53 series of compounds (M(OH)(bdc-R)(H_2O); M = Fe^{3+}, Al^{3+}; R = H, COOH, NH_2, OH).[14b] In this case the hydrophilic anchor points on the channel walls are located 7.2 Å apart and there is not a well ordered hydrogen bonding network observed within the solid-state structural characterization. This less-ordered arrangement of the water and lower density of anchor points may explain the smaller values for the proton conductivity for this material.

Values reported herein are also within range of other advanced inorganic and organic materials that are being evaluated for proton conductivity. A range of oxide based proton conductors, including perovskites, have been explored and conductivity values range from 1 x 10^{-8} to 1 x 10^{-2} S cm^{-1}.[21] Exceptionally high proton conductivity was also reported for Eu_2O_3 at 0.1 S cm^{-1}, but this value was reported at much higher temperatures (500 °C).[22] Within polymer and related organic composite materials, the proton conductivity is quite high at 10^{-2} to 10^{-1} S cm^{-1}.[23] Similarly, hybrid composites, such as those that contain Cd^{2+} coordination polymers imbedded in an organic polymer also possess high conductivity, with the largest value reported at 4.69 x 10^{-2} S cm^{-1} at 80 °C and 98% RH.[24]

Table 1. Conductivity, activation energy, and measurement conditions for reported water mediated proton-conducting MOFs and related modularly constructed porous solids. The hydrophobic/hydrophilic functional groups that are located on the surface of the interior channel walls are also detailed for each compound.

Compound	Conductivity [Scm^{-1}]	Activation energy [eV]	Measurement condition	Functional Groups/Hydrophobicity	Reference
Nafion	5×10^{-2}	0.22	25 °C, 100% RH	Hydrophobic backbone with sulfonic acid/strongly hydrophilic	[25]
$Cr_3(\mu_3\text{-}O)(H_2O)_3(NDC(SO_3H_{5/6})_2)_3$	1.27×10^{-1}	0.11	80° C, 100% RH	Internal surface is arranged with high-density sulfonic acid sites ($-SO_3H$)/strongly hydrophilic	[26]
$UiO\text{-}66(SO_3H)_2$	8.4×10^{-2}	0.32	80° C, 90% RH	Sulfonic acid linkers/strongly hydrophilic	[27]
$[Ni_2\text{-}(dobdc)(H_2O)_2]\cdot 6H_2O$	2.2×10^{-2}	0.12	80 °C, 95% RH	water molecules bound to Ni (II) nodes/ strongly hydrophilic	[28]
$[(CH_3)_2NH_2][In(cdc)(H\text{-}btc)]\cdot 2DMA\cdot 11H_2O$	1.80×10^{-2}	0.28	70 °C, RH not specified	COOH groups/ strongly hydrophilic	[17]
$[Pt(dach)(bpy)Br]_4(SO_4)_4\cdot 32H_2O$	1.7×10^{-2}	0.22	55 °C, 95% RH	Channel A: bpy linkers/ hydrophobic Channel B: sulfate/hydrophilic	[6d]
$(NH_4$ $(adp)[Zn_2(ox)_3]\cdot 3H_2O$	8.0×10^{-3}	0.63	25° C, 98% RH	ox (adp act as guest molecule and NH_4^+ act as counterion)/hydrophilic	[29]
$[Cd(C_{10}O_4N_3H_5)_2(C_2H_8N)_2(H_2O)]$ (Cd-5TIA)	3.61×10^{-3}	0.16	28 °C, 98% RH	carboxylic oxygen coordinated to Cd (III)/weakly hydrophilic	[30]
$Ba_2(HL^3)(H_2O)_4]$	2.9×10^{-3}	0.32	25° C, 99% RH	Carboxylic acid groups; hydrophilic	[12]

$([In(5\text{-}Hsip)_2(Me_2NH_2)]\cdot DMF\cdot(H_2O)_{1.4}$	1.25×10^{-3}		25° C, 40% RH	$Me_2NH_4^+$/hydrophilic	[8]
$(NH_4\ [MnCr_2\ (ox)_6]\ \cdot 4H_2\ O$	1.1×10^{-3}	0.23	RT, 96% RH	ox (NH_4^+ acts as counterion)/hydrophilic	[31]
Cu-LaMONT	*3.65×10^{-4}*	*0.65*	*25 °C, 95% RH*	*Carboxyl group; weakly hydrophilic*	*This work*
UMONT	*1.59×10^{-4}*	*0.15*	*25 °C, 95% RH*	*Uranyl oxo group; weakly hydrophobic*	*This work*
$[In(C_{10}O_4N_3H_5)_2(C_2H_8N)(H_2O)]$ (In-5TIA)	5.35×10^{-5}	0.14	28 °C, 98% RH	carboxylic oxygen coordinated to In(III)/weakly hydrophilic	[30]
$[Mo_5P_2O_{23}]\ [Cu(phen)\ (H_2O)]_3\cdot 5H_2O$	2.2×10^{-5}	0.23	28 °C, 98% RH	phen backbone and one ligated water/weakly hydrophobic	[32]
$M(OH)(bdc\text{-}(COOH)_2)(H_2O)$ (MIL-53)	0.7×10^{-5}	0.21	25° C, 95% RH	μ_2-OH and substituted functional groups/strongly hydrophilic	[14b]
$M(OH)(bdc\text{-}OH)\ (H_2O)$ (MIL-53)	4.2×10^{-7}	0.27	25° C, 95% RH	μ_2-OH and substituted functional groups /strongly hydrophilic	[14b]
$M(OH)(bdc\text{-}H)\ (H_2O)$ (MIL-53)	2.3×10^{-8}	0.47	25° C, 95% RH	μ_2-OH and substituted functional groups /strongly hydrophilic	[14b]
$M(OH)(bdc\text{-}NH_2)\ (H_2O)$	2.3×10^{-9}	0.45	25° C, 95% RH	μ_2-OH and substituted functional groups /strongly hydrophilic	[14b]

dach = (1R, 2R)-(–)-1,2-diaminocyclohexane, bpy = 4,4'-bipyridine, H_2dhbq = 2,5-dihydroxy-1,4-benzoquinone, 5TIA = 5-triazole isophthalic acid, adp = adipic acid, ox = oxalate , H_3btc = 1,3,5-benzene tricarboxylic acid, H_2cdc = 9H-carbazole-3,6-dicarboxylic acid, dobdc4- = 2,5-dioxido-1,4-benzenedicarboxylat, H_2bdc = 1,4-benzenedicarboxylicacid, H_5L_3 = ([1,1′:3′,1″-terphenyl]-2′,4,4′,4″,6′- pentacarboxylic acid, phen = phenanthroline, 5-H_3sip = 5-sulfoisophthalic acid, $Me_2NH_4^+$ = dimethylammonium cation, DMF = dimethylformamide

The other exception to the general trend for proton conductivity within MONT materials is $[Pt(dach)(bpy)Br]_4(SO_4)_4 \cdot 32H_2O$, with a value of 1.7×10^{-2} S cm^{-1} at 55 °C and 95% RH.[6d] In this particular material, there are two potential channels for proton conductivity: (1) Channel A is lined with bipyridine ligands and (2) Channel B that includes hydrophilic sulfate anions. An extended water network is located in channel A and strong hydrogen bonding occurs between the neighboring water molecules to create an extended network. Interactions between the confined water molecules and the inner pore for channel A is >2.9 Å, indicating weak interactions that lend evidence for the hydrophobic nature of the pore. Otake *et al*. performed quantum-mechanical molecular dynamics (QM-MD) simulations that indicated the fast proton transfer was occurring within the water networks of channel A because attractive interaction with the sulfate anions in channel B hindered the proton shuttling.

The channels within both Cu-LaMONT and UMONT can also be considered weakly hydrophobic. Within Cu-LaMONT, one water molecule is weakly bound to the inner channel wall at a donor to acceptor distance of 3.017 Å, while the remaining water molecules engage in hydrogen bonding between neighbors. For the UMONT system, the $-NH_2$ sites in the IDA ligands are oriented towards the exterior of the nanotube and may provide some electrostatic stability, but no direct hydrogen bonding capabilities.[33] The only available donor atom in proximity to OW2 (hydrogen atom of water) is the carboxylic oxygen, situated at distances of 3.386 Å, while in the OW1 site is the uranyl oxygen (poor hydrogen acceptor), located at distance of 3.05 Å.[10] In both cases, these subtle hydrogen bonding and electrostatic effects are enough to decrease the proton conductivity by ~10^2 compared to the $[Pt(dach)(bpy)Br]_4(SO_4)_4 \cdot 32H_2O$ system. This demonstrates the powerful effects that subtle changes can make in these hybrid materials containing extended 1-D water networks.

We also note that the proton conductivity within MONT materials with extended, ordered water networks is higher than what is observed for bulk phases but has some similarities to interfacial water. Conductivity within solid ice is quite low (10^{-8} to 10^{-10} S cm^{-1}) and values for liquid water are only slightly higher (10^{-6} to 10^{-7} S cm^{-1}).[34] Artemov *et al*. explored proton conductivity for interstitial water (1 nm thickness) located between nanograins of diamond and found that the values where higher (10^{-4} to 10^{-2} S cm^{-1}) than that of the bulk phase.[35] They reasoned that the increased conductivity for the interstitial water is related to both the higher mobility of the water at the surface and that the charge-carrying protons are not mutually screened, which is similar to effects expected within water confined within 1-D MONT materials.

Both UMONT and Cu-LaMONT display an increase in their proton conductivity as the temperature changes from 5 °C to 20 °C, followed by a rapid decrease to ~ 10^{-7} S cm^{-1}. We note that this phenomenon was also reported by Banerjee *et al.* for the In-5TIA and Cd-5TIA MONT systems.[30] This result can be explained by dehydration of the MONT material, as there is removal and dislocation of water molecules from the channel upon heating and a decrease in the overall proton conductivity. Previous work by Unruh *et al.* indicated dehydration of the confined water in UMONT system occur at 35 °C and the initiation of water removal in Cu-LaMONT has been observed approximately at 45 °C.[9c, 9d]

Activation energy of the proton conductivity can be utilized to understand the mechanism of the proton movement within the water channels.[3] When the E_a is between 0.1-0.4 eV, the proton conductivity mechanism is typically considered Grotthus-type because the protons move along a hydrogen bond network, which only requires energy to break and reform hydrogen bonds. With the vehicle mechanism the E_a is higher because it involves physical movement of protonated molecules, requiring more energy for the process. The calculated E_a value for UMONT (0.15 eV)

is similar to those reported for other hybrid materials with Grotthuss type proton hopping, where a protonic charge defect diffuses through the hydrogen bond network. The relatively high proton conductivity along the c-direction for UMONT could be ascribed to the high number of guest water molecules confined in the hydrophobic 1D hexagonal nanotubes. In addition, presence of strongly coordinated water molecules, for which various hydrogen-bonding interactions can be constructed to form a fast and efficient proton-transport pathway within the channel direction, could also result in proton conductivity through the Grotthuss mechanism.

The E_a for Cu-LaMONT is higher compared with typical hydrated proton conductors having the Grotthuss mechanism, such as Nafion (E_a = 0.22 eV)[36] and $UO_2HPO_4 \cdot 4H_2O$ (E_a = 0.32 eV)[37]. This suggests that the mechanism of proton conductivity for this material includes some other process, such as direct diffusion of additional protons with water molecules (vehicle mechanism) as reported by Xiang *et al* and Banerjee *et al*.[17, 30] At elevated temperatures, confined water molecules exhibit high kinetic energy, thereby facilitating rapid bond breaking and reforming within their network. While this increased mobility can enhance proton transport mechanisms, it may also result in shorter residence times for protons within the conducting pathways, thus limiting overall conductivity. As the temperature decreases, the reduced kinetic energy of water molecules results in the formation of a more stable and robust hydrogen bonding network. This strengthened network is associated with diminished proton conductivity due to the constrained mobility of water molecules at lower temperatures. Therefore, we hypothesize that for Cu-LaMONT the vehicle mechanism becomes more dominant than the Grotthuss proton conductivity as temperature increases from 5 °C to 20 °C.

CONCLUSION

This study evaluated the intricate relationship between molecular water arrangements and proton conductivity within two metal-organic nanotubes (UMONT and Cu-LaMONT) that contain relatively hydrophobic channel walls and ordered water networks within the pore spaces. At 95% relative humidity and ambient temperature, both systems demonstrated proton conductivity, with Cu-LaMONT exhibiting higher sensitivity to humidity changes. A temperature-dependent trend in proton conductivity was also noted, with UMONT showing higher values at lower temperatures due to its well-established hydrogen bonding network and hydrophobic interior pore wall. Comparisons with other reported materials underscore the significance of water interactions in influencing proton conduction. Both hydrophilic and hydrophobic materials can enhance proton conductivities, relying on either acidic functional group anchored to the channel walls or an extensive water network to provide the proton shuttle. The addition of weak hydrogen bonding or electrostatics within the pore wall of MONT materials, provided enough disruption to the water network to decrease the proton conductivity by 10^2 Scm^{-1}. The humidity and temperature dependency of these materials enables their use in applications such as sensing and catalysis. Further, activation energy calculations support the unique proton conduction mechanisms in these materials, suggesting the involvement of both Grotthuss and vehicle mechanisms. This comprehensive exploration underscores the intricate interdependence between material characteristics and proton conductivity, providing valuable insights for the purposeful design and optimization of porous hybrid systems.

EXPERIMENTAL METHODS

Synthetic Procedure

Copper nitrate trihydrate (99%, Acros Organics) lanthanide chloride septahydrate (99%, Alfa Aesar), piperazine (99%, Alfa Aesar), iminodiacetic acid (IDA; 99%, Alfa Aesar) ethanol (37%, Fisher Scientific), sodium hydroxide (97%, Fisher Scientific) and ammonium hydroxide (99%, Fisher Scientific) were used as received. Uranyl nitrate hexahydrate (98-102%; International Bio-Analytical Industries Inc.) was repurified before use in the synthesis of the UMONT material. CAUTION*: ^{238}U is a radioactive element and is handled by trained personnel in a licensed facility.* All stock solutions used in the synthesis of these compounds utilized Milli-Q (18 MΩ) water. Synthesis of the MONT materials have been previously reported but is summarized in the supporting information (SI) section I.[9c, 9d]

Crystallographic Characterization of Single Crystals

The identity of the compounds was confirmed by single-crystal X-ray diffraction before evaluating the impedance measurements for the crystalline material. A single crystal was isolated, coated in oil, placed in a MiTeGen mounting loop, and mounted on Bruker D8 Quest CCD single crystal X-ray diffractometer equipped with Mo Kα radiation (λ = 0.7107 Å) and a low temperature cryostat (Oxford Cryosystems, Cryostream 800). Initial data was collected at 100 K using APEX 4 software suite to confirm the quality of the single-crystal data. [18] Unit cell information for both materials is provided in Table S1. Dimensions of the crystals were measured using microscope camera feature associated with the Bruker D8 Venture Duo single crystal diffractometer and identification of crystal faces, particularly the (001) direction, was accomplished by employing the "Index Crystal Faces" functionality within the APEX4 software package.[18]

Characterization of sample purity

The bulk purity of the synthesized materials was confirmed through Powder X-ray diffraction analysis conducted with a Bruker D8 Advance diffractometer equipped with nickel-filtered Cu Kα

radiation (λ = 1.5418 Å). A zero-background silicon wafer was utilized to support approximately 10 mg of the ground sample, and a powder diffraction pattern was collected within a scan range of 5-60º 2θ, employing a step size of 0.05º. The purity was substantiated by comparing the experimental powder pattern with the calculated patterns generated from the crystallographic information file (CIF) using CrystalDiffract software within the CrystalMaker package (SI, Fig. S1 and S2).[38] The homogeneity of the metal content for the samples was also confirmed using a Hitachi S-3400N scanning electron microscope equipped with an EDS detector (SI, Fig. S3 and S4)

Electrochemical Impedance Spectroscopy Measurements

A custom-made glass chamber (SI, Fig. S5) was used to control the relative humidity (RH) and temperature for conductivity measurements. RH was monitored using the PTH450 sensor (precision ± 1.5%) developed by Dracal Technologies, and temperature was measured manually using a Fisherbrand™ thermometer that was directly inserted into the chamber. The entire glass chamber was immersed in a water bath to ensure uniform temperature distribution across the crystal sample and a thermometer was positioned near the crystal sample to provide the most accurate temperature measurements.

Oriented single crystals of the MONT materials were carefully glued to the Pt electrodes using conductive silver paste (SI, Fig S6). Electrochemical impedance spectroscopy (EIS) measurements were performed on the large single crystals of UMON and Cu-LaMONT using a CHI660E potentiostat. Impedance measurements of these single crystals were carried out by the conventional quasi-two-probe method using platinum electrodes and nickel wire (1 mmϕ). All measurement were done in the frequency range of 1 – 10^6 Hz and amplitude of 0.05 V using the CHI660E electrochemical workstation (CHI software version 17.02.).

Impedance Measurement of powder samples

Experiments were performed in the custom-made humidity controllable cell, at temperature 25 °C while humidity levels were changed from 75 to 95%. Both samples were finely ground to a powder using a mortar and pestle and the compacted pellet samples (UMONT: 0.72 mm x 0.60 mm x 0.21 mm; Cu-LaMONT: 0.51 mm x 0.62 mm x 0.18 mm) were prepared in a press. Measurements were performed by the conventional quasi two-probe method, using platinum electrodes and silver paste.

ACKNOWLEDGEMENT

We acknowledge support from the National Science Foundation Division of Materials Research (NSF-DMR15246700). The authors acknowledge Benjamin S. Revis for his support to design of glass chamber used in the impedance measurements and Dr. Scott Shaw for insights into the circuit models. Author also acknowledges Dr. Neil Spinner and Dr. Tim Paschkewitz from Pine Research for their support to finalize the circuits for EIS measurements. We also acknowledge the University of Iowa Materials, Analysis, Testing, and Fabrication facility for use of the powder X-ray diffractometer and scanning electron microscope.

REFERENCES

[1] aM. V. Nguyen, H. C. Dong, D. Nguyen-Manh, N. H. Vu, T. T. Trinh, T. B. Phan, *Journal of Science: Advanced Materials and Devices* **2021**, *6*, 509-515; bC. Dellago, M. M. Naor, G. Hummer, *Physical Review Letters* **2003**, *90*.
[2] N. Agmon, *Chemical Physics Letters* **1995**, *244*, 456-462.
[3] D.-W. Lim, M. Sadakiyo, H. Kitagawa, *Chemical science* **2019**, *10*, 16-33.
[4] aC. Li, G. A. Voth, *Proceedings of the National Academy of Sciences* **2021**, *118*, e2113141118; bH. Kandori, Y. Yamazaki, J. Sasaki, R. Needleman, J. K. Lanyi, A.

Maeda, *Journal of the American Chemical Society* **1995**, *117*, 2118-2119; cT. Loerting, K. R. Liedl, *The Journal of Physical Chemistry A* **2001**, *105*, 5137-5145.
[5] aT. Min, R. Zhang, L. Chen, Q. Zhou, *Encyclopedia* **2023**, *3*, 746-758; bM. M. Tellez-Cruz, J. Escorihuela, O. Solorza-Feria, V. Compañ, *Polymers* **2021**, *13*, 3064; cQ. Liu, Z. Li, D. Wang, Z. Li, X. Peng, C. Liu, P. Zheng, *Frontiers in Chemistry* **2020**, *8*, 694.
[6] aK. Mochizuki, K. Koga, *Proceedings of the National Academy of Sciences* **2015**, *112*, 8221-8226; bA. J. Rieth, K. M. Hunter, M. Dincă, F. Paesani, *Nature communications* **2019**, *10*, 4771; cS. Chakraborty, H. Kumar, C. Dasgupta, P. K. Maiti, *Accounts of chemical research* **2017**, *50*, 2139-2146; dK.-I. Otake, K. Otsubo, T. Komatsu, S. Dekura, J. M. Taylor, R. Ikeda, K. Sugimoto, A. Fujiwara, C.-P. Chou, A. W. Sakti, Y. Nishimura, H. Nakai, H. Kitagawa, *Nature Communications* **2020**, *11*.
[7] S.-L. Zheng, C.-M. Wu, L.-H. Chung, H.-Q. Zhou, J. Hu, Z. Liu, Y. Wu, L. Yu, J. He, *ACS Energy Letters* **2023**, *8*, 3095-3101.
[8] B. Joarder, J.-B. Lin, Z. Romero, G. K. H. Shimizu, *Journal of the American Chemical Society* **2017**, *139*, 7176-7179.
[9] aA. Tinti, A. Giacomello, Y. Grosu, C. M. Casciola, *Proceedings of the National Academy of Sciences* **2017**, *114*, E10266-E10273; bF.-X. Coudert, A. Boutin, A. H. Fuchs, *Communications Chemistry* **2021**, *4*; cD. K. Unruh, K. Gojdas, A. Libo, T. Z. Forbes, *Journal of the American Chemical Society* **2013**, *135*, 7398-7401; dY. P. Ren, L. S. Long, B. W. Mao, Y. Z. Yuan, R. B. Huang, L. S. Zheng, *Angewandte Chemie* **2003**, *115*, 550-553; eM.-L. Chen, Y.-C. Guo, F. Yang, J.-X. Liang, Z.-X. Cao, Z.-H. Zhou, *Dalton Transactions* **2014**, *43*, 6026; fF. Dai, H. He, D. Sun, *Inorganic Chemistry* **2009**, *48*, 4613-4615.
[10] T. H. Jahinge, M. K. Payne, D. K. Unruh, A. S. Jayasinghe, P. Yu, T. Z. Forbes, *Langmuir* **2023**.
[11] C. Zhang, D. G. Knyazev, Y. A. Vereshaga, E. Ippoliti, T. H. Nguyen, P. Carloni, P. Pohl, *Proceedings of the National Academy of Sciences* **2012**, *109*, 9744-9749.
[12] P. Rought, C. Marsh, S. Pili, I. P. Silverwood, V. G. Sakai, M. Li, M. S. Brown, S. P. Argent, I. Vitorica-Yrezabal, G. Whitehead, M. R. Warren, S. Yang, M. Schröder, *Chemical Science* **2019**, *10*, 1492-1499.
[13] E. Freier, S. Wolf, K. Gerwert, *Proceedings of the National Academy of Sciences* **2011**, *108*, 11435-11439.
[14] aA. De, O. Basu, T. Basu, R. Mondal, *Crystal Growth & Design* **2021**, *21*, 1461-1472; bA. Shigematsu, T. Yamada, H. Kitagawa, *Journal of the American Chemical Society* **2011**, *133*, 2034-2036.
[15] J.-G. Jia, L.-M. Zheng, *Coordination Chemistry Reviews* **2020**, *403*, 213083.
[16] L. C. Applegate, T. Z. Forbes, *CrystEngComm* **2020**, *22*, 3406-3418.
[17] Q. Lin, Y. Ye, L. Liu, Z. Yao, Z. Li, L. Wang, C. Liu, Z. Zhang, S. Xiang, *Nano Research* **2021**, *14*, 387-391.
[18] T. Francart, A. Van Wieringen, J. Wouters, *Journal of neuroscience methods* **2008**, *172*, 283-293.
[19] A. S. Jayasinghe, M. K. Payne, D. K. Unruh, A. Johns, J. Leddy, T. Z. Forbes, *Journal of Materials Chemistry A* **2018**, *6*, 1531-1539.
[20] V. S. S. Tiron H.L. Jahinge, Tori Z. Forbes, (Ed.: U. o. Iowa), Manucript In preparation, **2024**.

[21] U. Tariq, M. Z. Khan, O. Gohar, Z. U. Din Babar, F. Ali, R. A. Malik, I. A. Starostina, Samia, J. Rehman, I. Hussain, M. Saleem, A. Ghaffar, M. A. Marwat, K. Zheng, M. Motola, M. B. Hanif, *Journal of Power Sources* **2024**, *613*, 234910.
[22] S. Wan, M. A. K. Y. Shah, H. Wang, P. D. Lund, B. Zhu, *iScience* **2024**, *27*, 108612.
[23] P. Wei, Y. Sui, X. Meng, Q. Zhou, *Journal of Applied Polymer Science* **2023**, *140*, e53919.
[24] M. Das Dawn, S. Roy, A. Garai, S. Banerjee, K. Biradha, *ChemSusChem*, *n/a*, e202401463.
[25] A. H. R.C.T Slade, P.G Dickens, *Solid State Ionics* **1983**, *9–10*, 1093-1098.
[26] F. Yang, G. Xu, Y. Dou, B. Wang, H. Zhang, H. Wu, W. Zhou, J.-R. Li, B. Chen, *Nature Energy* **2017**, *2*, 877-883.
[27] W. J. Phang, H. Jo, W. R. Lee, J. H. Song, K. Yoo, B. Kim, C. S. Hong, *Angewandte Chemie International Edition* **2015**, *54*, 5142-5146.
[28] W. J. Phang, W. R. Lee, K. Yoo, D. W. Ryu, B. Kim, C. S. Hong, *Angewandte Chemie International Edition* **2014**, *53*, 8383-8387.
[29] M. Sadakiyo, T. Yamada, H. Kitagawa, *J AM CHEM SOC* **2009**, *131*, 9906-9907.
[30] T. Panda, T. Kundu, R. Banerjee, *Chemical Communications* **2012**, *48*, 5464.
[31] E. Pardo, C. Train, G. Gontard, K. Boubekeur, O. Fabelo, H. Liu, B. Dkhil, F. Lloret, K. Nakagawa, H. Tokoro, S.-I. Ohkoshi, M. Verdaguer, *Journal of the American Chemical Society* **2011**, *133*, 15328-15331.
[32] C. Dey, T. Kundu, R. Banerjee, *Chem. Commun.* **2012**, *48*, 266-268.
[33] M. K. Payne, M. M. Pyrch, M. Jubinsky, M. C. Basile, T. Z. Forbes, *Chemical Communications* **2018**, *54*, 10828-10831.
[34] V. G. Artemov, *Physical Chemistry Chemical Physics* **2019**, *21*, 8067-8072.
[35] V. G. Artemov, E. Uykur, P. O. Kapralov, A. Kiselev, K. Stevenson, H. Ouerdane, M. Dressel, *The Journal of Physical Chemistry Letters* **2020**, *11*, 3623-3628.
[36] aK.-D. Kreuer, S. J. Paddison, E. Spohr, M. Schuster, *Chemical Reviews* **2004**, *104*, 4637-4678; bG. Alberti, M. Casciola, *Solid State Ionics* **2001**, *145*, 3-16; cR. Slade, A. Hardwick, P. Dickens, *Solid State Ionics* **1983**, *9*, 1093-1098.
[37] aL. Bernard, A. Fitch, A. Wright, B. Fender, A. Howe, *Solid State Ionics* **1981**, *5*, 459-462; bA. T. Howe, M. G. Shilton, *Journal of Solid State Chemistry* **1979**, *28*, 345-361.
[38] D. C. Palmer, (Ed.: C. S. Ltd), Begbroke, Oxfordshire, England, **2014**.

TABLE OF CONTENT

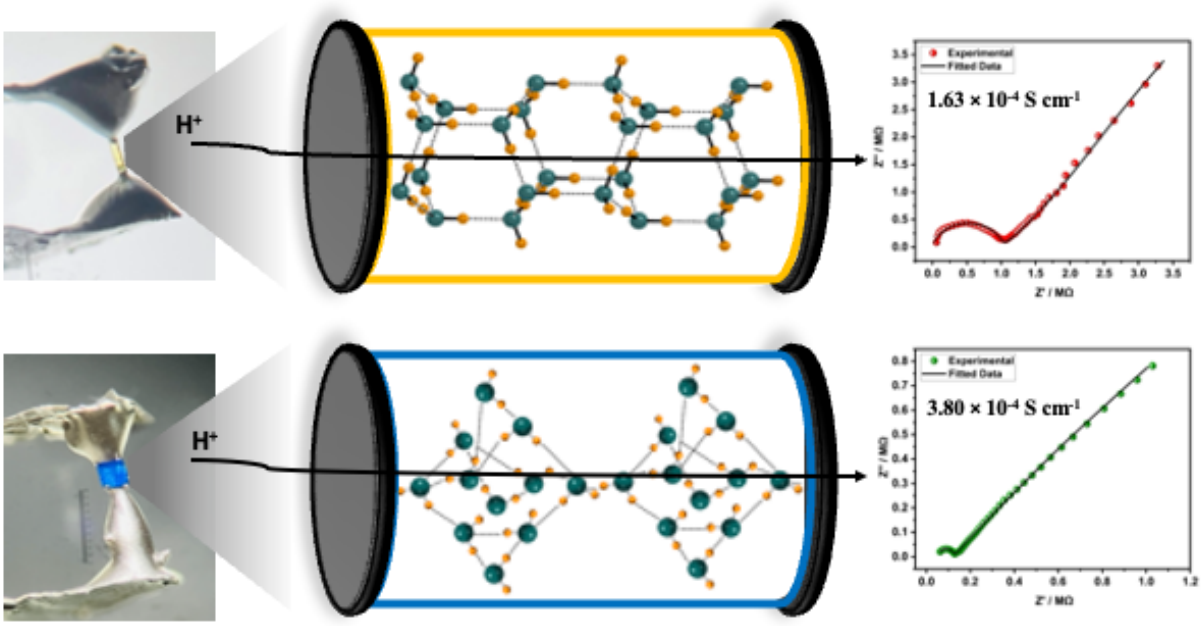

Proton conductivity in single crystals of hydrated metal organic nanotubes (MONT) were evaluated using electrochemical impedance spectroscopy. Water-wall interactions within the crystals influences the overall conductivity and the anisotropic behavior of the conductivity through the 1-D channels was confirmed through oriented studies on oriented single crystals of the MONT materials.